EARTHQUAKE ENGINEERING AND STRUCTURAL DYNAMICS, VOL. 18, 999–1016 (1989)

DEPENDENCE OF FOURIER SPECTRUM AMPLITUDES OF RECORDED EARTHQUAKE ACCELERATIONS ON MAGNITUDE, LOCAL SOIL CONDITIONS AND ON DEPTH OF SEDIMENTS

M. D. TRIFUNAC

Civil Engineering Department, Denny Research Building 394, University of Southern California, Los Angeles, CA 90089–1114, USA

SUMMARY

New empirical scaling equations of Fourier amplitude spectra of strong earthquake shaking are presented for the site characterization in terms of local geologic and local soil conditions simultaneously. It is shown that using only the local soil site classification may lead to biased results, and it is suggested that both soil and geologic conditions should be used together in estimation of the site specific spectrum amplitudes.

INTRODUCTION

The possibility that the local site conditions influence the amplitudes of recorded seismic waves have been investigated by many researchers. This has been studied theoretically[1–3] and experimentally [4–9] by considering various overall measures of strong shaking or its effects on different types of structures. In the 1960's and 1970's these studies took on a more detailed and more complete nature because of the increased availability of recorded strong motion accelerograms. Through comparison of the shapes of the Fourier and response spectrum amplitudes, it became possible to describe the effects the local soil conditions have on the local site response[10] and to extend the results of Gutenberg[6] about the effects of the local geologic conditions to the high frequency spectral amplitudes.[11] Through the 1970's and early 1980's these studies were refined by detailed regression analyses which were made possible by still larger numbers of well documented records of strong ground motion.[11–15]

To this date these studies considered either the local soil or the local geologic site conditions and never combined the simultaneous effects of both media in the development of one or more general scaling relations. Since the typical dimensions of the local soil versus the local geologic site conditions are so different, one might expect that their effects would be reflected in the recorded spectral amplitudes in high and in low frequencies respectively. If both of these effects can be shown to contribute significantly to the variation of spectral amplitudes between 0·05 and 25 Hz, the frequency range of interest to earthquake engineering, then both soil and geologic site conditions should be considered simultaneously. The purpose of this paper is to analyse this and to show how these effects could be used in the empirical scaling of Fourier amplitude spectra.

SCALING OF FOURIER SPECTRA IN TERMS OF M, R, H, S, h, s_L and v

The current model

Trifunac and Lee[14] recently studied the scaling of Fourier amplitude spectra FS(T) in terms of magnitude M, source-to-station distance R, focal depth H, 'size' of fault S, component orientation v, and local geology, characterized by the representative depth of sediments h (or by the local geological site parameter s). Their scaling relation takes the form

$$\log_{10} \mathrm{FS}(T) = M + \mathscr{A}\mathrm{tt}(\Delta, M, T) + b_1(T)M + b_2(T)h + b_3(T)v + b_5(T) + b_6(T)\mathrm{M}^2 \qquad (1)$$

0098–8847/89/070999–18$09.00

Received 3 October 1988
Revised 22 March 1989

They did not include the term $b_4(T)\Delta$ because it was found to be insignificant. Here $\mathscr{A}\mathrm{tt}(\Delta, M, T)$ is the new frequency dependent attenuation function. It is of the form[13]

$$\mathscr{A}\mathrm{tt}(\Delta, M, T)=\begin{cases}\mathscr{A}_0(T)\log_{10}\Delta & R\leqslant R_0\\ \mathscr{A}_0(T)\log_{10}\Delta_0-(R-R_0)/200 & R>R_0\end{cases} \tag{2}$$

with Δ, the representative source-to-station distance, given by

$$\Delta=S\ln\left[\frac{R^2+H^2+S^2}{R^2+H^2+S_0^2}\right]^{-1/2} \tag{3}$$

and

$$\Delta=S\ln\left[\frac{R_0^2+H^2+S^2}{R_0^2+H^2+S_0^2}\right]^{-1/2} \tag{4}$$

S_0 is the coherence radius of the source.[16] The term $\mathscr{A}_0(T)\log_{10}\Delta$ is used to calculate the attenuation function at distances R less than some transition distance R_0, where $\Delta=\Delta_0$. For distances $R>R_0$, the attenuation becomes a linear function of distance R with slope equal to $-1/200$; R_0 is[13]

$$R_0=\frac{1}{2}\left(\frac{-200\mathscr{A}_0(T)(1-S_0^2/S^2)}{\ln 10}+\sqrt{\frac{200\mathscr{A}_0(T)(1-S_0^2/S^2)}{\ln 10}-4H^2}\right) \tag{5}$$

and is a function of H, S, S_0 and $\mathscr{A}_0(T)$. Replacing the Richter empirical attenuation function[17] with the frequency dependent attenuation function above has not only contributed the additional flexibility for estimating the Fourier spectral amplitudes, but also has decreased the residuals of actual relative to the model predictions, relative to our earlier regression models.[11, 12]

Updating the database

The database of Trifunac and Lee[14] consists of 438 free-field records with 3 components each, from 104 earthquakes for the years from 1933 to 1983. Table I presents the list of all earthquakes in this database. It contains information on the name, date and time of each earthquake, the latitude and longitude of its epicentre, its focal depth, local magnitude and maximum intensity, if available. Each of the 438 free-field records is accompanied by the information on the address of the recording station, the latitude and longitude of the station, the local Modified Mercalli Intensity that has been reported for the station site or estimated[18] and the local geology classification characterized by the site parameter s or the depth of alluvium h. This list of earthquakes has been updated now to a total of 106, with the addition of two recent earthquakes, the Coalinga earthquake of 1983 and the Morgan Hill earthquake of 1984, both in California. With the addition of 56 free-field records from these two earthquakes, the total number of free-field records is now 494.

To proceed with the present analysis, information on the soil site properties has been collected from various available sources, including different reports of the United States Geological Survey (U.S.G.S.), California Division of Mines and Geology (C.D.M.G), Nuclear Regulatory Comission, university reports and various consulting reports. At first these data have been characterized by a soil parameter s_L, which was assigned values 1 for deep soil sites, 2 for stiff soil sites and 3 for 'rock' sites.[19] Subsequently, this characterization was changed to 0 for 'rock' sites, 1 for stiff soil sites and 2 for deep soil sites, for convenience in regression analysis.

The new regression analysis

To include the soil classification in the regression analysis, the regression equation of the Fourier amplitudes will now take the form

$$\begin{aligned}\log_{10}\mathrm{FS}(T)=M+\mathscr{A}\mathrm{tt}(\Delta, M, T)+b_1(T)M+b_2(T)h+b_3(T)v+b_4(T)hv+b_5(T)\\ +b_6(T)M^2+b_7^{(1)}(T)S_L^{(1)}+b_7^{(2)}(T)S_L^{(2)}\end{aligned} \tag{6}$$

Equation (6) is of the same form as equation (1), but with the addition of the new terms $b_4(T)hv$, $b_7^{(1)}(T)S_L^{(1)}$ and $b_7^{(2)}(T)S_L^{(2)}$. The terms $b_4(T)hv$ and $b_2(T)h$ will result in the factor multiplying the depth of alluvium h to

Table I

1	3	10	1933	1754PST	33	37	00	−177	58	00	16.0	6·3	9	Long Beach, CA
2	10	2	1933	0110PST	33	47	00	−118	08	00	16·0	5·4	6	Southern California
3	7	6	1934	1449PST	41	42	00	−124	36	00			5	Eureka, CA
4	12	30	1934	0552PST	32	15	00	−115	30	00	16·0	6·5	9	Lower California
5	10	31	1935	1138MST	46	37	00	−111	58	00		6·0	8	Helena, MT
6	10	31	1935	1218MST	46	37	00	−111	58	00			3	Helena, MT
7	11	21	1935	2058MST	46	36	00	−112	00	00			6	Helena, MT
8	11	28	1935	0742MST	46	37	00	−111	58	00			6	Helena, MT
9	2	6	1937	2042PST	40	30	00	−125	15	00			5	Humboldt Bay, CA
10	4	12	1938	0825PST	32	53	00	−115	35	00	16·0	3.0		Imperial Valley, CA
11	6	5	1938	1842PST	32	54	00	−115	13	00	16·0	5·0		Imperial Valley, CA
12	6	6	1938	0435PST	32	15	00	−115	10	00	16·0	4·0		Imperial Valley, CA
13	9	11	1938	2210PST	40	18	00	−124	48	00		5·5	6	NW California
14	5	18	1940	2037PST	32	44	00	−115	30	00	16·0	6·7	10	Imperial Valley, California
15	2	9	1941	0145PST	40	42	00	−125	24	00		6·4		NW California
16	6	30	1941	2351PST	34	22	00	−119	35	00	16·0	5·9	8	Santa Barbara, California
17	10	3	1941	0813PST	40	36	00	−124	36	00		6·4	7	Northern California
18	11	14	1941	0042PST	33	47	00	−118	15	00	16·0	5·4	8	Torrance-Gardena, CA
19	10	21	1942	0822PST	32	58	00	−116	00	00	16·0	6·5	7	Borrego Valley, California
20	3	9	1949	0429PST	37	06	00	−121	18	00		5·3	7	Northern CA
21	4	13	1949	1156PST	47	06	00	−122	42	00		7·1	8	Western Wash
22	1	23	1951	2317PST	32	59	00	−115	44	00	16·0	5·6	7	Imperial Vally, CA
23	10	7	1951	2011PST	40	17	00	−124	48	00		5·8	7	NW California
24	7	21	1952	0453PDT	35	00	00	−119	01	00	16·0	7·7	11	Kern County, California
25	7	23	1952		35	17	00	−118	39	00				Kern County, CA
26	9	22	1952	0441PDT	40	12	00	−124	25	00		5·5	7	Northern California
27	11	21	1952	2346PST	35	50	00	−121	10	00		6·0	7	Southern California
28	6	13	1953	2017PST	32	57	00	−115	43	00	16·0	5·5	7	Imperial Valley, CA
29	1	12	1954	1534PST	35	00	00	−119	01	00	16·0	5·9	8	Wheeler Ridge, CA
30	4	25	1954	1233PST	36	48	00	−121	48	00		5·3	7	Central California
31	11	12	1954	0427PST	31	30	00	−116	00	00	16·0	6·3	5	Lower California
32	12	21	1954	1156PST	40	47	00	−123	52	00		6·5	7	Eureka, CA
33	9	4	1955	1801PST	37	22	00	−121	47	00		5·8	7	San Jose, CA
34	12	16	1955	2117PST	33	00	00	−115	30	00	16·0	4·3		Imperial County, CA
35	12	16	1955	2142PST	33	00	00	−115	30	00	16·0	3·9		Imperial County, CA
36	12	16	1955	2207PST	33	00	00	−115	30	00	16·0	5·4	7	Imperial County, CA
37	2	9	1956	0633PST	31	42	00	−115	54	00	16·0	6·8		El Alamo, Baja CA
38	2	9	1956	0725PST	31	42	00	−115	54	00		6·4		El Alamo, Baja CA
39	3	18	1957	1056PST	34	07	06	−119	13	12	13·8	4·7	6	Southern California
40	3	22	1957	1048PST	37	40	00	−122	28	00		3·8	5	San Francisco, CA
41	3	22	1957	1144PST	37	40	00	−122	29	00		5·3	7	San Francisco, CA
42	3	22	1957	1515PST	37	39	00	−122	27	00		4·4	5	San Francisco, CA
43	3	22	1957	1627PST	37	39	00	−122	29	00		4·0	5	San Francisco, CA
44	1	19	1960	1926PST	36	47	00	−121	26	00		5·0	6	Central California
45	6	5	1960	1718PST	40	49	00	−124	53	00		5·7	6	Northern California
46	4	8	1961	2323PST	36	30	00	−121	18	00	11·0	5·7	7	Hollister, CA
47	9	4	1962	0917PST	40	58	00	−124	12	00		5·0	6	Northern California
48	4	29	1965	0729PST	47	24	00	−122	18	00		6·5	8	Puget Sound, WA
49	7	15	1965	2346PST	34	29	06	−118	31	18	15·1	4·0	6	Southern California
50	6	27	1966	2026PST	35	57	18	−120	29	54	6·0	5·6	7	Parkfield, CA
51	8	7	1966	0936PST	31	48	00	−114	30	00	16·0	6·3	6	Gulf of California
52	9	12	1966	0841PST	39	24	00	−120	06	00		6·3	7	Northern California
53	12	10	1967	0407PST	40	30	00	−124	36	00		5·8	6	Northern California
54	12	18	1967	0925PST	37	00	36	−121	47	18		5·2	6	Northern California
55	4	8	1968	1830PST	33	11	24	−116	07	42	11·1	6·4	7	Borrego Mtn, CA
56	9	12	1970	0630PST	34	16	12	−117	32	24	8·0	5·4	7	Lytle Creek, CA
57	2	9	1971	0600PST	34	24	42	−118	24	00	13·0	6·4	11	San Fernando, CA
58	10	15	1979	1417PST	32	37	59	−115	19	59	12·0	6·6		Imperial Valley, CA
59	8	6	1979	0805PST	37	06	43	−121	31	59	9·6	5·9		Coyote Lake, CA

Table I (*contd.*)

60	8	13	1978	2254GMT	34	21	04	−119	42	00	12·5	5·5	Santa Barbara, CA
61	1	24	1980	1100PST	37	49	37	−121	47	13	5·9	5·9	Mt. Diablo, Livermore, CA
62	1	26	1980	1833PST	37	45	00	−121	42	47	7·3	5·2	Mt. Diablo, Livermore, CA
63	08	02	1975	2022GMT	39	26	58	−121	28	25	4·1	5·2	Oroville, Aftershock
64	08	02	1975	2059GMT	39	26	00	−121	28	31	5·1	5·2	Oroville, Aftershock
65	08	03	1975	0103GMT	39	29	19	−121	30	59	8·8	4·6	Oroville, aftershock
66	08	03	1975	0247GMT	39	28	52	−121	30	21	7·4	4·1	Oroville, aftershock
67	08	05	1975	0228GMT	39	24	18	−121	29	43	6·2	3·2	Oroville, aftershock
68	08	06	1975	0350GMT	39	29	46	−121	31	49	9·2	4·7	Oroville, aftershock
69	08	06	1975	1641GMT	39	29	31	−121	31	45	9·7	3·9	Oroville, aftershock
70	08	03	1975	0700GMT	39	29	50	−121	30	41	7·7	4·8	Oroville, aftershock
71	08	11	1975	0611GMT	39	27	29	−121	28	59	3·1	4·4	Oroville, aftershock
72	08	11	1975	1559GMT	39	30	20	−121	31	35	9·8	3·8	Oroville, aftershock
73	08	16	1975	0548GMT	39	28	12	−121	31	42	8·5	4·1	Oroville, aftershock
74	08	16	1975	1223GMT	39	29	52	−121	30	16	7·1	3·1	Oroville, aftershock
75	09	27	1975	2234GMT	39	31	12	−121	31	56	10·4	4·6	Oroville, aftershock
76	11	28	1974	2301GMT	36	54	0	−121	30	0	9·0	0·	6 Hollister, CA
77	1	11	1975	1737PST	40	13	12	−124	15	36	2·0	4·7	6 Northern California
78	5	6	1975	1835PST	40	16	48	−124	40	12	0·	4·0	Northern California
79	6	7	1975	0846GMT	40	34	12	−124	08	24	21·0	5·7	7 Northern California
80	3	8	1971	1508PST	35	40	0	−118	24	12	6·0	4·7	5 Central California
81	5	2	1971	0608GMT	51	24	0	−177	12	0	43·0	7·1	6 Andreanof, AK
82	9	12	1971	1132PST	41	17	54	−123	40	24	20·0	4·6	5 Northern California
83	7	30	1972	2145GMT	56	49	12	−135	40	48	25·0	7·1	7 Southeast Alaska
84	9	4	1972	1804GMT	36	38	13	−121	17	13	2·0	4·8	6 Central California
85	5	26	1980	1857GMT	37	32	37	−118	51	41	2·8	4·9	Mammoth aftershock
86	5	27	1980	1450GMT	37	27	49	−118	49	24	2·4	6·3	Mammoth aftershock
87	5	27	1980	1901GMT	37	36	15	−118	46	11	3·8	5·0	Mammoth aftershock
88	5	28	1980	0516GMT	37	34	49	−118	53	09	3·3	4·8	Mammoth aftershock
89	5	31	1980	1516GMT	37	32	22	−118	54	22	8·2	5·1	Mammoth aftershock
90	6	11	1980	0441GMT	37	30	24	−119	02	34	14·1	5·0	Mammoth aftershock
91	6	28	1980	0058GMT	37	33	23	−118	51	45	5·1	4·1	Mammoth aftershock
92	10	16	1979	1616PDT	33	4	29	−115	33	16	5·0	4·9	Imperial Valley aft
93	10	16	1979	1445PDT	33	2	44	−115	29	24	3·9	4·6	Imperial Valley aft
94	10	16	1979	1114PDT	32	58	19	−115	36	22	4·7	4·2	Imperial Valley aft
95	10	15	1979	2319GMT	32	46	0	−115	26	29	9·5	5·0	Imperial Valley aft
96	4	26	1981	1209GMT	33	7	48	−115	39	0	8·0	5·6	Westmoreland, CA
97	1	24	1980	1900GMT	37	50	24	−121	48	0	5·9	5·9	Livermore, CA
98	1	26	1980	0233GMT	37	45	36	−121	42	0	7·3	5·2	Livermore, CA
99	5	25	1980	0934PDT	37	36	32	−118	50	49	9·0	6·1	Mammoth aftershock
100	5	25	1980	0949PDT	37	37	41	−118	55	37	14·0	6·0	Mammoth aftershock
101	5	25	1980	1245PDT	37	33	40	−118	49	52	16·0	6·1	Mammoth aftershock
102	5	25	1980	1336PDT	37	37	30	−118	51	32	2·0	5·7	Mammoth aftershock
103	5	26	1980	1158PDT	37	32	35	−118	53	17	5·0	5·7	Mammoth aftershock
104	5	27	1980	0751PDT	37	30	22	−118	49	34	14·0	6·2	Mammoth aftershock
105	5	2	1983	1642PDT	36	15	00	−120	16	48	9·0	6·5	Coalinga earthquake
106	4	24	1984	1315PST	37	19	01	−121	40	48	9·0	6·2	Morgan Hill earthquake

be component dependent, so that for horizontal components with $v=0$, and vertical components with $v=1$, it takes the form

$$b_2(T)h+b_4(T)hv=(b_2(T)+b_4(T)v)h=\begin{cases}b_2(T)h; & v=0\\ (b_2(T)+b_4(T))h; & v=1\end{cases} \tag{7}$$

The addition of the other two terms, $b_7^{(1)}(T)S_L^{(1)}$ and $b_7^{(2)}(T)S_L^{(2)}$, is to characterize the soil at the site, where

$$S_L^{(1)}=\begin{cases}1 \text{ if } s_L=1 \text{ (stiff soil)}\\ 0 \text{ otherwise}\end{cases}$$

and

$$S_L^{(2)} = \begin{cases} 1 & \text{if } s_L = 2 \text{ (deep soil)} \\ 0 & \text{otherwise} \end{cases} \tag{8}$$

The use of the two variables $S_L^{(1)}$ and $S_L^{(2)}$ instead of one for s_L is because s_L is a qualitative or categorical variable which takes on the discrete values of 0, 1 and 2 for three distinct types of soil classification. It is thus different from all the other variables used, like magnitude or depth, h, which are quantitative variables, that is, variables with a well defined scale of measurement. It is thus necessary to use indicator variables to account for the different levels of the classification[20].

Database selection for regression analysis

The database selection procedure for the Fourier amplitude data, FS(T), is essentially the same as that in our previous analysis.[14] The data are partitioned into six groups corresponding to magnitude ranges 2·0–2·9, 3·0–3·9, 4·0–4·9, 5·0–5·9, 6·0–6·9 and 7·0–7·9. Then each of these magnitude ranges is subdivided first according to the site classifications[14] of $s = 0$, 1 and 2. The data within one magnitude range and one site classification are then further subdivided according to the soil classifications $s_L = 0$, 1 and 2. Finally, the data within each of these subgroups are separated into two sets according to component orientation: one set for horizontal ($v = 0$) and one set for vertical ($v = 1$). To balance properly the effects of attenuation at small and large distances, the data in each of the subsets are further subdivided into 2 groups: one for epicentral distances $\leqslant 100$ km and the other for distances > 100 km. The data in each of these two final subsets are then arranged, in increasing order in terms of their amplitudes. If the number of data in the first group ($R \leqslant 100$ *km*) is less than 19, all the data points are kept. Otherwise at most 19 points are selected from among the ordered set of data so that they correspond uniformly, as close as possible, to the 5th, 10th, . . . , up to the 95th percentiles. Similarly, at most 5 points are selected for the second group ($R > 100$ km) of data so that they correspond uniformly to around the 1/6, 1/3, 1/2, 2/3 and 5/6 × 100th percentiles. The above selection process is repeated for each of the 91 periods in the range 0·04 to 15 sec. In addition, at the long period end, data points with amplitudes that are smaller than the average digitization noise, i.e. those with signal-to-noise ratio less than one, are automatically elimated from the selection process.

The fitted coefficients at each period T resulting from linear regression will be denoted by $\hat{b}_1(T)$, $\hat{b}_2(T)$, $\hat{b}_3(T)$, $\hat{b}_4(T)$, $\hat{b}_5(T)$, $\hat{b}_6(T)$, $\hat{b}_7^{(1)}(T)$, $\hat{b}_7^{(2)}(T)$ [see equation (6)] respectively. For given values of T, h, v, Δ and s_L, $\log_{10}$ FS(T) represents a parabola when plotted versus M. Following our preceding analyses[14] it is again assumed here that equation (6) applies only in the range $M_{min} \leqslant M \leqslant M_{max}$ where, for each period T:

$$M_{min}(T) = -\hat{b}_1(T)/(2\hat{b}_6(T))$$

and

$$M_{max}(T) = -(1 + \hat{b}_1(T))/(2\hat{b}_6(T)) \tag{9}$$

For $M \leqslant M_{min}$, M is used only in the first term of equation (6) and M_{min} is used with b_1 (T) and b_6 (T). For $M \geqslant M_{max}$, M_{max} is used in all the terms for M.

Results of the regression analysis

Figure 1 shows $\hat{b}_1(T)$ to $\hat{b}_6(T)$, $\hat{b}_7^{(1)}(T)$ and $\hat{b}_7^{(2)}(T)$ as full lines, and the corresponding estimates of the 90 per cent confidence intervals represented by the dashed lines. The coefficients for M, $\hat{b}_1(T)$ and M^2, $\hat{b}_6(T)$ are both significant in practically the whole period range considered except possibly at the short and long period ends. Note that this is in good agreement with the conclusions of our previous analysis,[14] where it was shown that the Fourier amplitudes do not just grow linearly with magnitude. It is noted here that the coefficient multiplying the depth of alluvium h, $\hat{b}_2(T)$, remains positive all through the period range and is essentially significant for all periods T, including the high frequency (low period) end. This is again in agreement with our previous analyses for both Fourier amplitudes[14] and pseudo relative velocity amplitudes,[15] PSV(T), at all five damping values. The coefficient for the component direction v, $\hat{b}_3(T)$, is also in agreement with previous analyses. The new coefficient for hv, $\hat{b}_4(T)$, which was not considered in our previous work is negative in the whole period range and is significant in the mid period range. It is significant, with 90 per cent confidence, in

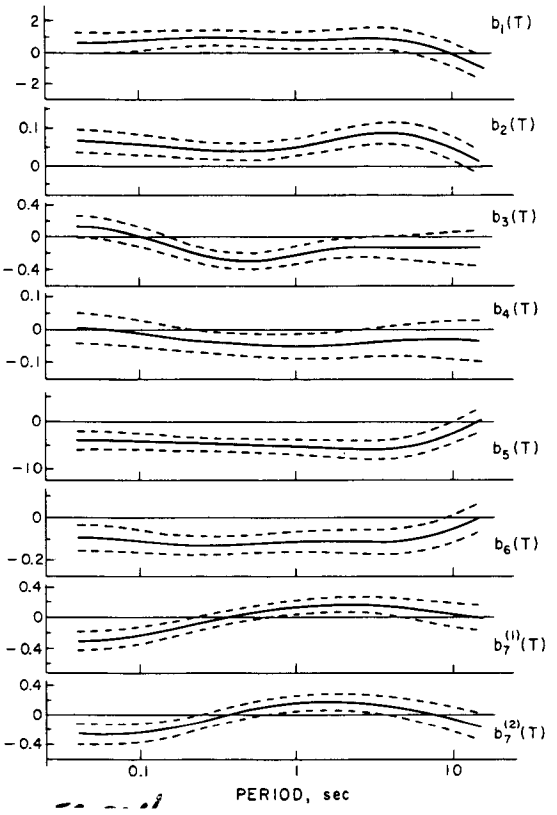

Figure 1. Functions $\hat{b}_1(T)$ to $\hat{b}_7^{(2)}(T)$ (full lines) in equation (6) and the estimates of their 90 per cent confidence intervals (dashed lines)

the range from 0·25 to 2·5 sec. This term should thus be included in all subsequent analyses of Fourier and response amplitudes. The coefficient for the constant term, $\hat{b}_6(T)$, is also in agreement with our previous work and is significant essentially in the whole period range. Finally, the new coefficients, $b_7^{(1)}(T)$ and $\hat{b}_7^{(2)}(T)$, corresponding to the indicator variables $S_L^{(1)}(s_L=1)$ and $S_L^{(2)}(s_L=2)$, show an interesting trend. For periods up to 0·35 sec both are negative and then become positive up to 10 sec periods. This means that in the period range below $\sim$0·35 sec the Fourier amplitudes are attenuated and between 0·35 and 10 sec, the Fourier amplitudes are amplified.

With FS(T) representing the Fourier amplitude spectra computed from recorded accelerograms, the residues are calculated from

$$\varepsilon(T)=\log_{10}[\mathrm{FS}(T)]-\log_{10}[\widehat{\mathrm{FS}}(T)] \tag{10}$$

It is assumed that $\varepsilon(T)$ can be described by a normal distribution function with mean $\mu(T)$ and standard deviation $\sigma(T)$ as follows:

$$p(\varepsilon,T)=\frac{1}{\sigma(T)\sqrt{2\pi}}\int_{-\infty}^{\varepsilon(T)}\exp\left[-\frac{1}{2}\left(\frac{x-\mu(T)}{\sigma(T)}\right)^2\right]dx \tag{11}$$

where $p(\varepsilon, T)$ represents the probability that $\log_{10}[\mathrm{FS}(T)-\log_{10}[\widehat{\mathrm{FS}}(T)]\leqslant\varepsilon(T)$. For a given residual value $\varepsilon(T)$ at particular period T, the actual probability $p^*(\varepsilon, T)$ that $\varepsilon(T)$ will not be exceeded can be evaluated by finding the fraction of residuals $\varepsilon(T)$ (computed from the database at the particular period) which are smaller than the given value.

Using equation (11), the estimated probability $\hat{p}(\varepsilon, T)$ that $\varepsilon(T)$ will not be exceeded can also be evaluated and compared with the above fractions. For $p^*(\varepsilon, T)$ calculated at 91 periods, the residuals $\varepsilon(T)$ corresponding

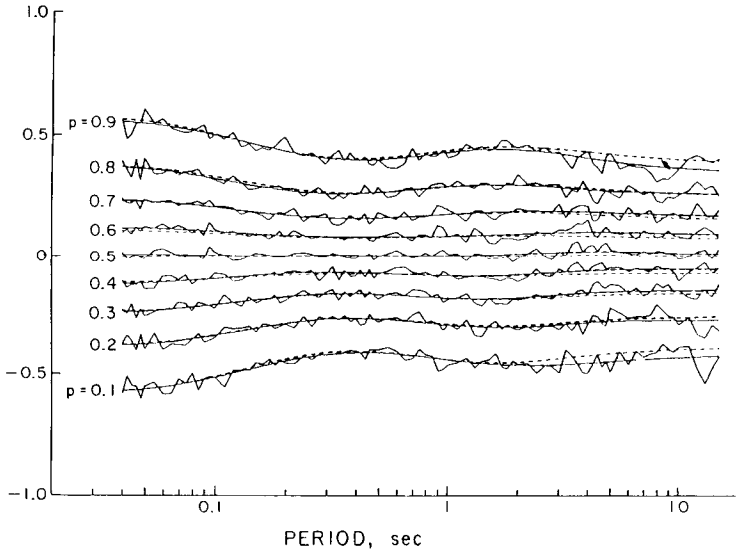

Figure 2. Distribution of residuals (irregular full lines and smooth full lines) relative to the scaling model equation (6). Smooth dashed lines represent $p(\varepsilon, T)$ computed from equation (11) as an approximation to the $p^*(\varepsilon, T)$ (full lines)

to $p^* = 0{\cdot}1, 0{\cdot}2, \ldots, 0{\cdot}8$ and $0{\cdot}9$ are plotted in Figure 2. The nine sets of curves, plotted versus period T from bottom to top correspond to the residual values at each of the probability levels 0·1 to 0·9. At each such level, the rough solid line represents the actual calculated residue values. The smooth solid curves are obtained by smoothing the rough solid curves along the period (T) axis. The smooth surface, $p^*(\varepsilon, T)$, from the nine solid curves thus represents the distribution of the computed Fourier amplitudes FS(T) about the estimated amplitudes $\widehat{\text{FS}}(T)$ given in equation (6). By fitting $p(\varepsilon, T)$ in equation (11) to $p^*(\varepsilon, T)$ at 91 periods, the mean and standard deviation of the normal distribution function, $\hat{\mu}(T)$ and $\hat{\sigma}(T)$, are evaluated. Substituting these values into equation (11), with $p(\varepsilon, T)$ taking values 0·1 to 0·9, will result in $\hat{\varepsilon}(T)$ for the nine probability levels. These are the nine dashed lines in Figure 2. The surface $p^*(\varepsilon, T)$ that resulted from the new regression model in the present analysis is narrower in the ε range when compared with that of our previous analyses.[11, 12, 14, 21, 22, 23]

Figure 3 shows a plot of the statistical parameters. The smooth amplitudes of $\hat{\mu}(T)$ and $\hat{\sigma}(T)$ and their 95 per cent confidence intervals are repectively given in the top two plots of the figure. The two full curves in the bottom of the figure are the smoothed amplitudes of the computed χ^2, $\chi^2(T)$ and Kolmogorov–Smirnov, KS(T), statistics. The dashed lines are their corresponding 95 per cent cutoff levels. It is seen that in the whole period range considered, both the χ^2 and K–S tests fail to reject the hypothesis that the distribution is normal. The density function in equation (11) thus represents an acceptable approximation to $p^*(\varepsilon, T)$.

Table II presents, for 12 periods, between $T = 0{\cdot}04$ sec and $T = 14$ sec, the values of the smoothed regression coefficients $\hat{b}_1(T)$, $\hat{b}_2(T)$, $\hat{b}_3(T)$, $\hat{b}_4(T)$, $\hat{b}_5(T)$, $\hat{b}_6(T)$, $\hat{b}_7^{(1)}(T)$, $\hat{b}_7^{(2)}(T)$, $M_{\min}(T)$, $M_{\max}(T)$, the nine smoothed calculated residue levels corresponding to $p^*(\varepsilon, T) = 0{\cdot}1$ to 0·9, the smoothed coefficients $\hat{\mu}(T)$, $\hat{\sigma}(T)$, in equation (11) and the χ^2 and the Kolmogorov–Smirnov statistics. The 12 periods presented will be sufficient for most practical computations, especially since the smoothness of the coefficients is such that any interpolation scheme will yield adequate estimates of FS(T) in the entire period range, from 0·04 to 14 sec.

Examples of estimated Fourier spectra

Figure 4 presents four plots of estimated FS(T) spectra using equation (6). The top two plots are examples of FS(T) computed for magnitudes $M = 4{\cdot}5$, 5·5, 6·5 and 7·5 at epicentral distance $R = 0$, focal depth $H = 5$ km, soil parameter $s_L = 1$ (stiff soil), for $p(\varepsilon, T) = 0{\cdot}5$ [equation (11)], and for horizontal and vertical motions. The solid lines in both plots correspond to the depth of sediments $h = 0$ km, while the dashed lines correspond to

Table II. $\log_{10}\mathrm{FS}(T)=M_{<}+\mathscr{A}\mathrm{tt}(\Delta, M, T)+b_1(T)M_{<>}+b_2(T)h+b_3(T)v+b_4(T)hv+b_5(T)+b_6(T)M^2_{<>}+b_7^{(1)}(T)S_L^{(1)}+b_7^{(2)}(T)S_L^{(2)}$

Period, T(sec)	0·040	0·065	0·11	0·19	0·34	0·50	0·90	1·60	2·80	4·40	7·50	14·0
Coefficients.												
$b_1(T)$	0·652	0·667	0·819	0·962	0·977	0·927	0·854	0·876	0·940	0·856	0·382	−0·707
$b_2(T)$	0·067	0·063	0·056	0·047	0·040	0·039	0·049	0·067	0·084	0·087	0·069	0·020
$b_3(T)$	0·127	0·091	−0·012	−0·155	−0·272	−0·292	−0·233	−0·152	−0·122	−0·126	−0·132	−0·131
$b_4(T)$	0·006	−0·002	−0·015	−0·030	−0·041	−0·047	−0·051	−0·048	−0·040	−0·033	−0·030	−0·034
$b_5(T)$	−3·921	−3·876	4·151	−4·532	−4·809	−4·924	−5·151	−5·568	−5·881	−5·529	−3·791	−0·019
$b_6(T)$	−0·095	−0·098	−0·114	−0·127	−0·128	−0·123	−0·112	−0·110	−0·113	−0·110	−0·080	−0·006
$b_7^{(1)}(T)$	−0·314	−0·282	−0·219	−0·120	−0·008	0·052	0·120	0·161	0·161	0·127	0·065	−0·002
$b_7^{(2)}(T)$	−0·264	−0·260	−0·238	−0·151	−0·012	0·069	0·144	0·169	0·152	0·103	0·004	−0·144
$M_{\min}$	3·429	3·389	3·604	3·780	3·810	3·773	3·814	3·991	4·155	3·897	2·376	0.000
$M_{\max}$	8·691	8·472	8·006	7·711	7·711	7·845	8·282	8·549	8·576	8·450	8·600	14·500
Residues:												
$p=0·1$	−0·568	−0·549	−0·504	−0·450	−0·413	−0·411	−0·435	−0·459	−0·461	−0·451	−0·436	−0·425
$p=0·2$	−0·378	−0·363	−0·330	−0·291	−0·267	−0·269	−0·290	−0·303	−0·293	−0·281	−0·274	−0·272
$p=0·3$	−0·240	−0·227	−0·203	−0·176	−0·162	−0·165	−0·178	−0·182	−0·169	−0·156	−0·150	−0·147
$p=0·4$	−0·121	−0·112	−0·096	−0·080	−0·073	−0·077	−0·086	−0·086	−0·074	−0·064	−0·061	−0·059
$p=0·5$	0·007	0·006	0·003	0·002	0·003	0·002	0·001	0·005	0·015	0·020	0·016	0·009
$p=0·6$	0·123	0·117	0·104	0·092	0·084	0·083	0·086	0·093	0·100	0·103	0·100	0·094
$p=0·7$	0·236	0·225	0·201	0·176	0·162	0·163	0·175	0·187	0·189	0·185	0·178	0·170
$p=0·8$	0·367	0·349	0·314	0·277	0·259	0·265	0·286	0·296	0·285	0·272	0·264	0·257
$p=0·9$	0·557	0·535	0·491	0·436	0·398	0·396	0·421	0·439	0·423	0·397	0·372	0·354
Residue statistics:												
$\mu(T)$	−0·002	−0·002	−0·002	−0·001	−0·001	−0·001	−0·002	−0·001	0·002	0·003	0·001	−0·001
$\sigma(T)$	0·445	0·426	0·388	0·343	0·316	0·317	0·338	0·352	0·343	0·328	0·315	0·305
$\chi^2(T)$	8·634	8·319	7·075	6·625	7·147	7·322	7·173	8·148	10·442	11·722	11·514	10·936
$\mathrm{KS}(T)$	0·032	0·032	0·031	0·030	0·031	0·031	0·031	0·034	0·040	0·044	0·046	0·046

$M_{<}=\min(M, M_{\max})$, $M_{<>}=\max(M_{\min}, \mathrm{M}_{<})$

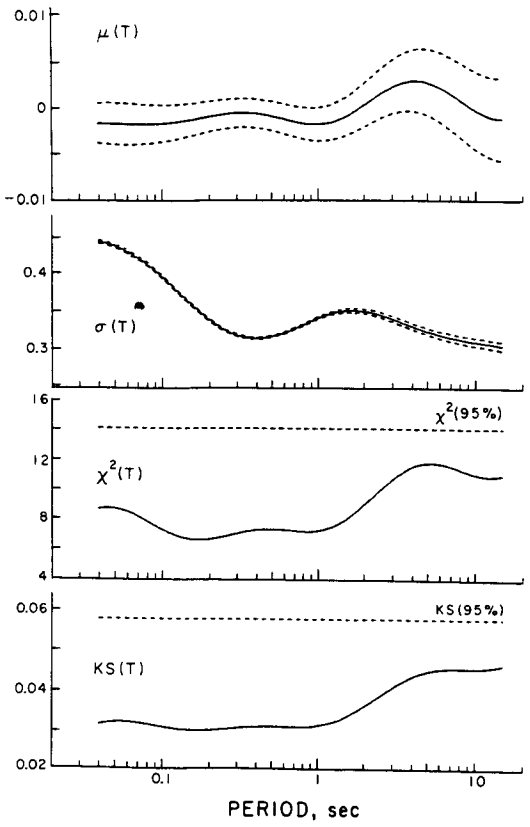

Figure 3. $\hat{\mu}(T)$ and $\hat{\sigma}(T)$ in equation (11) (full lines) and their 95 per cent confidence intervals (top two diagrams). Actual (full lines) and permissible (dashed lines), with 95 per cent confidence, amplitudes of the $\chi^2(T)$ and Kolmogorov–Smirnov KS(T) tests are shown in the bottom two diagrams

that of $h=4$ km. The lower left figure illustrates the effect of epicentral distance R on the changes of spectral amplitudes for magnitude $M=6{\cdot}5$, focal depth $H=5$ km, sedimentary depth $h=2$ km, soil parameter $s_L=1$, $p(\varepsilon)=0{\cdot}5$ and for horizontal (solid lines) and vertical (dashed lines) components. Four sets of curves corresponding to $R=0$, 25, 50 and 100 km are presented. The lower right plot in this figure illustrates the effect of focal depth H on the changes of spectral amplitudes for $p(\varepsilon, T)=0{\cdot}5$, $M=6{\cdot}5$, $R=0$ km, $h=2$ km and $s_L=1$ for both horizontal (solid) and vertical (dashed) components.

The diagonal dashed lines at the bottom of each plot in this and in all subsequent similar figures represent the average FS amplitude of the digitization and processing noise. The plot of each FS spectrum is presented only for those periods where the signal-to-noise ratios are not much less than unity, or where the slope of a curve in the log–log scale is not significantly greater than -1.

The trends of the computed FS(T) amplitudes in the figures presented here (Figure 4) are in many ways similar to those discussed in our previous analyses.[21] The top two sets of graphs show that, as before, the rate of growth of amplitudes with magnitudes M decreases as M approaches 7·5. The effect of local geologic conditions (alluvial depth) is significant for the whole range of periods from 0·04 to 14 sec for both horizontal and for vertical motions. This is now different from what we found in our previous analyses, where the geologic site characteristics were found to play an important role only at intermediate and long periods and no significant role at high frequencies. This difference can be attributed to the new form of the dependence of the site characteristics in the present analysis [equation (7)] on h and v simultaneously:

$$b_2(T)h+b_4(T)hv=(b_2(T)+b_4(T)v)h \tag{12}$$

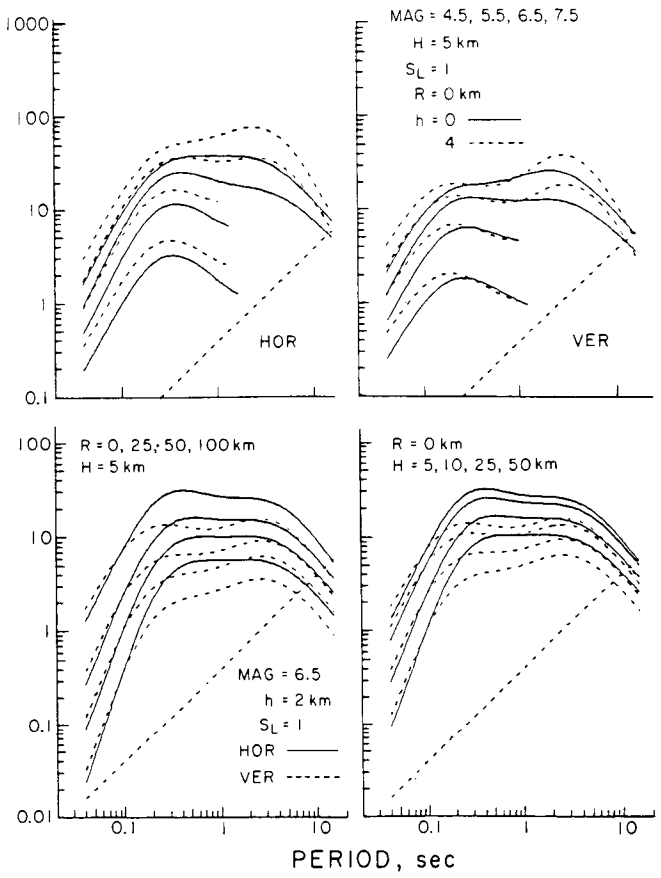

Figure 4. *Top*: Estimated Fourier amplitude spectra (in/sec), $p(\varepsilon, T)=0{\cdot}5$ for $M=4{\cdot}5$, 5·5, 6·5 and 7·5, alluvium depth $h=0$ km (full lines) and 4 km (dashed lines) for focal depths $H=5$ km, stiff soil sites $s_L=1$, zero epicentral distance ($R=0$ km) and for horizontal (left) and vertical (right motions. *Bottom*: Estimated Fourier amplitude spectra (in/sec), $p(\varepsilon, T)=0{\cdot}5$, for $M=6{\cdot}5$, $h=2$ km, horizontal (full lines) and vertical (dashed lines) motion, and stiff soil ($s_L=1$). Left: Focal depth $H=5$ km and epicentral distances $R=0$, 25, 50 and 100 km. Right: Epicentral distance $R=0$ km and focal depth $H=5$, 10, 25 and 50 km*

which results in the coefficient for the site characteristics being component dependent. These new trends are also dependent on the simultaneous consideration of soil and geologic site conditions.

Figure 5 presents another four plots of estimated FS(T) amplitudes, to illustrate the effect of local soil conditions on FS(T). The top two plots are examples of FS(T) computed for magnitudes $M=4{\cdot}5$, 5·5, 6·5 and 7·5 at epicentral distance $R=0$, focal depth $H=5$ km, alluvial depth $h=2$ km, for $p(\varepsilon, T)=0{\cdot}5$, and for the horizontal ($v=0$) and vertical ($v=1$) motions. The solid lines in both plots correspond to the local soil condition $s_L=0$ (rock) while the dashed lines in both plots correspond to $s_L=2$ (deep soil). The bottom two plots show examples of FS(T) for magnitude $M=6{\cdot}5$, epicentral distances $R=0$, 25, 50 and 100 km, focal depth $H=5$ km, alluvial depth $h=2$ km, for $p(\varepsilon, T)=0{\cdot}5$, and for horizontal ($v=0$) and vertical ($v=1$) motions. The solid lines again correspond to $s_L=0$ and the dashed lines to $s_L=2$. In each set of the graphs, it is observed that, for periods up to ~0·35 sec, the Fourier amplitudes FS(T) at 'rock' sites ($s_L=0$) are higher than those at deep soil sites ($s_L=2$). Beyond 0·35 sec, this trend is reversed up to the periods of about 10 sec so that, for these intermediate periods, the Fourier amplitudes at deep soil sites are higher than those at the rock sites.

Figures 6 and 7 compare the differences of the effects the local geologic and local soil site characteristics have on FS(T). Figure 6 consists of three plots, one for each local soil classification ($s_L=0$, 1 and 2). For each

*1 in/sec = 0·0254 m/sec.

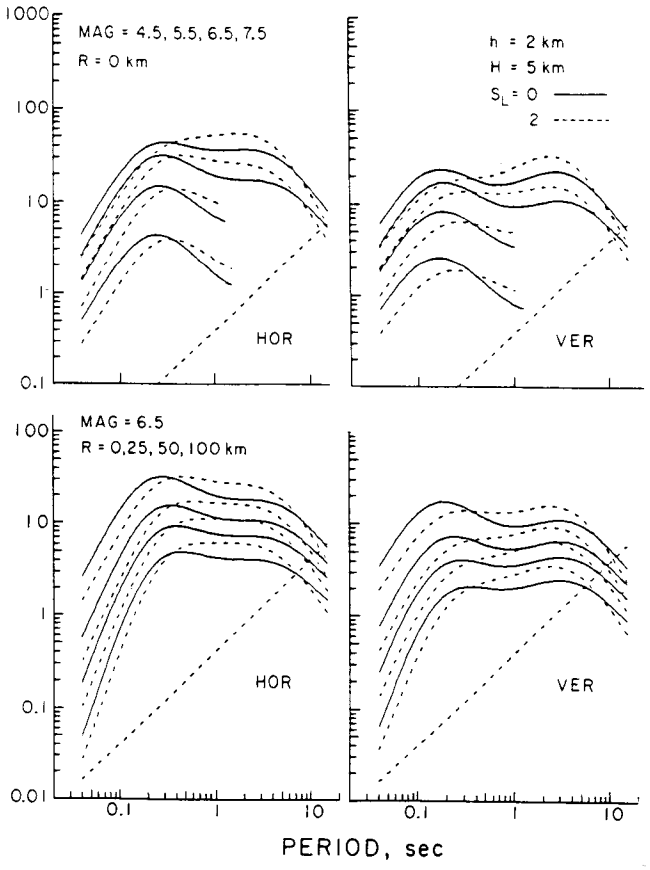

Figure 5. *Top*: Estimated Fourier amplitude spectra (in/sec), $p(\varepsilon, T)=0{\cdot}5$ for $M=4{\cdot}5, 5{\cdot}5, 6{\cdot}5$ and $7{\cdot}5$, alluvium depth $h=2$ km epicentral distance $R=0$ km, focal depths $H=5$ km for 'rock' sites $s_L=0$ (full lines) and deep soil sites, $s_L=2$ (dashed lines). *Bottom*: Estimated Fourier amplitude spectra (in/sec), $p(\varepsilon, T)=0{\cdot}5$ for $M=6{\cdot}5$, epicentral distances $R=0$, 25, 50 and 100 km, focal depth $H=5$ km, alluvium depth $h=2$ km, 'rock' sites $s_L=0$ (full lines) and deep soil sites $s_L=2$ (dashed lines) for horizontal (left) and vertical (right) motions

plot, FS(T) has been computed for the depth of alluvium equal to 0, 2 and 4 km. This figure shows that, for all local soil site classifications, in the whole period range considered, the greater the alluvial depth, the higher will be the Fourier amplitudes. Figure 7 also shows three plots, one for each alluvial depth equal to 0, 2 and 4 km. For each alluvium depth, the soil classification ranges from $s_L=0$ (rock) to 1 (still soil) and to 2 (deep soil). It is seen that for periods up to $\sim 0{\cdot}3$ sec the Fourier amplitudes FS(T) on $s_L=0$ (rock) sites are higher than those with $s_L=1$ (stiff soil) or $s_L=2$ (deep soil). Beyond $\sim 0{\cdot}3$ sec, this trend is reversed up to periods of about 10 sec, a trend also indicated earlier in Figure 5. The two figures (6 and 7) show that local alluvium depth and local soil parameters have different characteristics at different period ranges and that both are significant but in a different way.

Actual versus estimated Fourier spectra

Figure 8 shows an example of how horizontal and vertical Fourier spectra computed from equation (6) compare with the actual Fourier spectra for the corresponding components of recorded strong-motion data. The record reference name of the file used here (AA001) corresponds to the standard accelerogram file name in the uniform database[24] used in this work. In Figure 8 the $\log_{10}$ FS(T) spectra were computed for the probability of exceedance $p(\varepsilon, T)=0{\cdot}1, 0{\cdot}5$ and $0{\cdot}9$. The interval between the spectra for $p=0{\cdot}1$ and $0{\cdot}9$ then represents an estimate of the 80 per cent confidence interval. As can be seen from this figure, the agreement between the recorded and the estimated spectra is good.

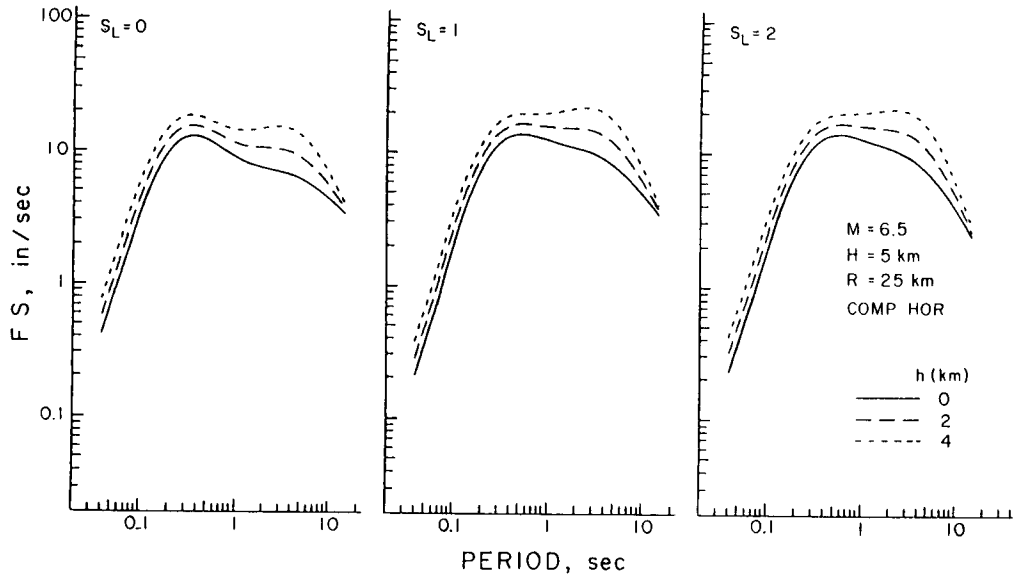

Figure 6. Estimated Fourier amplitude spectra, $p(\varepsilon, T)=0{\cdot}5$ for $M=6{\cdot}5$, source depth $H=5$ km, epicentral distance $R=25$ km, horizontal motions and depths of sediments $h=4$ km (short dashed lines), 2 km (long dashed lines) and 0 km (full lines) for 'rock' sites $s_L=0$ (left), stiff soil sites $s_L=1$ (centre) and deep soil sites $s_L=2$ (right)

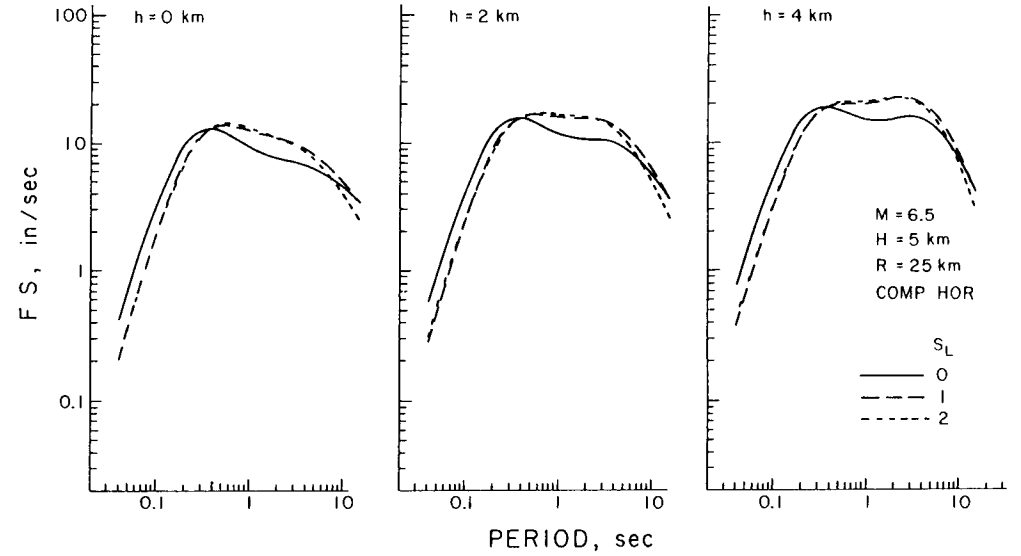

Figure 7. Estimated Fourier amplitude spectra, $p(\varepsilon, T)=0{\cdot}5$, for $M=6{\cdot}5$, source depth $H=5$ km, epicentral distance $R=25$ km, horizontal motions and 'rock' sites $s_L=0$ (full lines), stiff soil sites $s_L=1$ (long dashed lines) and deep soil sites $s_L=2$ (short dashed lines) for depth of sediments $h=0$ km (left), $h=2$ km (centre) and $h=4$ km (right)

The residue two-step model

The previous sections in this paper dealt with the direct, '1-step' model where the scaling of Fourier spectra in terms of M, R, H, S, h, s_L and v has been performed in one step, with the soil indicator variables included in the regression equation directly. Here we consider another alternative in which the previous regression model[21, 23] [equation (1)] which does not include soil classification may have already been developed and the

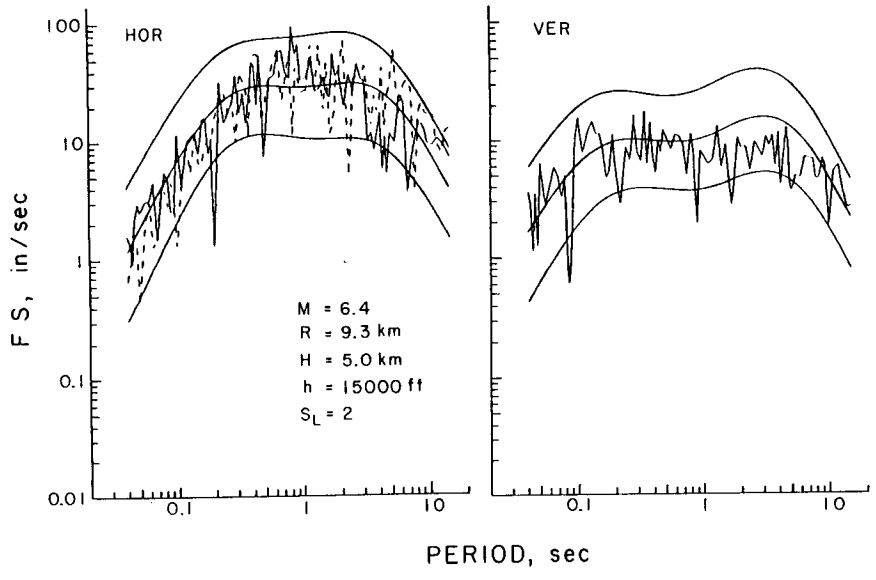

Figure 8. Comparison of actual (AA001, El Centro 1940, $M=6{\cdot}4$, $R=9{\cdot}3$ km, $H=5$ km, $h=15{,}000$ feet (4·57 km), $s_L=2$) and estimated Fourier spectrum amplitudes for $p(\varepsilon, T)=0{\cdot}1$, 0·5 and 0·9 and for horizontal (left) and vertical (right) motion

scaling functions $\hat{b}_1(T)$ to $\hat{b}_6(T)$ estimated. To study the influence that the additional soil classification may have on the Fourier spectral amplitudes, the residues with respect to that regression model can first be calculated:

$$\varepsilon(T)=\log_{10}\mathrm{FS}(T)-\log_{10}\widehat{\mathrm{FS}}(T) \tag{13}$$

with $\log_{10}\mathrm{FS}(T)$ representing the actual Fourier amplitudes. The residues at each site where soil classification is available can then be fitted by the equation

$$\varepsilon(T)=b_7^{(1)}(T)S_L^{(1)}+b_7^{(2)}(T)S_L^{(2)}+b_8(T) \tag{14}$$

where $S_L^{(1)}$ and $S_L^{(2)}$ are the indicator variables for s_L as defined previously, $b_7^{(1)}(T)$ and $b_7^{(2)}(T)$ are corresponding scaling functions and $b_8(T)$ is a new additional 'constant coefficient'. Equation (1) can now be combined with equation (14) to become

$$\begin{aligned}\log_{10}\widehat{\mathrm{FS}}(T)=M_<+\mathscr{A}\mathrm{tt}(\Delta, M, T)+\hat{c}_1(T)M_{<>}+\hat{c}_2(T)h+\hat{c}_3(T)v+\hat{c}_4(T)hv+\hat{c}_5(T)\\ +\hat{c}_6(T)M_{<>}^2+\hat{c}_7^{(1)}(T)S_L^{(1)}+\hat{c}_7^{(2)}(T)S_L^{(2)}\end{aligned} \tag{15}$$

where

$$M_<=\min(M, M_{\max})$$

and

$$M_{<>}=\max(M_{\min}, M_<)$$

and $\hat{c}_i(T)=\hat{b}_i(T)$ except for the scaling function $\hat{c}_5(T)$ for the constant 1, which is

$$\hat{c}_5(T)=\hat{b}_5(T)+\hat{b}_8(T) \tag{16}$$

The variance of $\hat{c}_5(T)$, $\hat{\sigma}_{c5}(T)$, is given by the root-mean-square of the variances of $\hat{b}_5(T)$ and $\hat{b}_8(T)$:

$$\hat{\sigma}_{c5}(T)=(\hat{\sigma}_{b5}^2(T)+\hat{\sigma}_{b8}^2(T))^{1/2} \tag{17}$$

This procedure can be referred to as the residues '2-step' model in contrast with the direct '1-step' model presented earlier. Detailed comparisons of corresponding results of the direct '1-step' model and the residues

'2-step' model show a lot of similarity between the two analyses.[23] The shapes of the scaling functions are very similar, the residues for the nine probability levels have almost identical widths and the estimated FS amplitudes are also very similar. One advantage that the residues '2-step' model has over the direct '1-step' model is that, in the '2-step' model, the first step of regression [equation (1)] can be performed on a larger database including sites where information on soil classification is absent. It is only in the second step [equation (14)] that regression has to be performed on that part of the database for the sites with available soil classification. Thus as more information on soil site classification becomes available, only the second step of iteration needs to be repeated to update the scaling functions. As for the direct '1-step' model, the regression analysis can be performed only on that part of the database which corresponds to the sites with data on soil classification. Every time this part of the database is updated, the whole regression has to be repeated.

SCALING OF FOURIER SPECTRA IN TERMS OF THE LOCAL SOIL CLASSIFICATION ONLY

The scaling equation: Magnitude, distance and soil classification

The preceding parts of this paper have presented the scaling of Fourier amplitude spectra in terms of magnitude, source-to-station representative distance, local geological site characterization, local soil site classification and for horizontal and vertical component directions. This part deals with the following question: What will happen to the scaling of Fourier amplitude spectra if the local site is characterized only by the local soil classification and no geological characterization is to be included? Seed *et al.*[19] carried out such a study for the scaling of response spectra, using only the local soil classification. Subsequently, other analyses have been carried out along similar lines. With a larger database now available, it is interesting to see how different such scaling will be if compared with the results in the preceding parts of this work. The scaling equation now becomes

$$\log_{10}\mathrm{FS}(T)=M+\mathscr{A}\mathrm{tt}(\Delta, M, T)+b_1(T)M+b_3(T)v+b_5(T)+b_6(T)M^2 +b_7^{(1)}(T)S_L^{(1)}+b_7^{(2)}(T)S_L^{(2)} \tag{18}$$

Here the equation is in the same form as equation (6) except that the $b_2(T)$ term for h and $b_4(T)$ term for hv are dropped. The scaling functions $b_1(T)$, $b_3(T)$, $b_5(T)$, $b_6(T)$, $b_7^{(1)}(T)$ and $b_7^{(2)}(T)$ are determined through the regression analysis of the same database as in the previous section. The scaling functions computed from linear regression will be denoted by $\hat{b}_1(T)$ to $\hat{b}_7^{(2)}(T)$, respectively.

Substituting the fitted coefficients in equation (18) gives $\widehat{\mathrm{FS}}(T)$, the extimated spectral amplitudes. As before equation (18) applies only in the rage $M_{\min}\leqslant M\leqslant M_{\max}$, and can be modified to

$$\log_{10}\widehat{\mathrm{FS}}(T)=M_{<}+\mathscr{A}\mathrm{tt}(\Delta, M, T)+\hat{b}(\mathrm{T})\mathrm{M}_{<>}+\hat{b}_3(T)v+\hat{b}_5(T)+\hat{b}_6(T)M^2_{<>} +\hat{b}_7^{(1)}(T)S_L^{(1)}+\hat{b}_7^{(2)}(T)S_L^{(2)} \tag{19}$$

The regression coefficients

Figure 9 shows the smoothed coefficients $\hat{b}_1(T)$, $\hat{b}_3(T)$, $\hat{b}_5(T)$, $\hat{b}_6(T)$, $\hat{b}_7^{(1)}(T)$ and $\hat{b}_7^{(2)}(T)$ (solid lines) together with the estimates of their 90 per cent confidence intervals (dashed lines). It is interesting to compare this figure with the corresponding Figure 1 where the local site geological condition in terms of the local alluvium depth is included in the regression analysis. The comparison shows that the scaling functions $\hat{b}_1(T)$, $\hat{b}_3(T)$, $\hat{b}_5(T)$ and $\hat{b}_6(T)$ corresponding respectively to the parameters M, v, 1 and M^2 are similar both in shape and in amplitudes on both figures. The scaling functions $b_7^{(1)}(T)$, $\hat{b}_7^{(2)}(T)$ for the soil parameters $s_L^{(1)}$ ($s_L=1$) and $s_L^{(2)}$ ($s_L=2$) are similar only in shape but exhibit differences in amplitudes. The scaling function $\hat{b}_7^{(2)}(T)$ for $S_L^{(2)}$ in Figure 1 has amplitudes around $-0{\cdot}25$ for periods less than 0·1 sec. Beyond 0·35 sec it is positive, but is not higher than about 0·15 in the period range 0·35 to 3 sec. On the other hand, the scaling function $\hat{b}_7^{(2)}(T)$ for $S_L^{(2)}$ in the present model (Figure 9) has amplitudes close to $-0{\cdot}1$ for periods less than 0·1 sec. Beyond 0·3 sec it turns positive and has amplitudes as high as 0·3 around period $T=5$ sec. Comparison of the scaling function $\hat{b}_7^{(1)}(T)$ leads to similar observations.

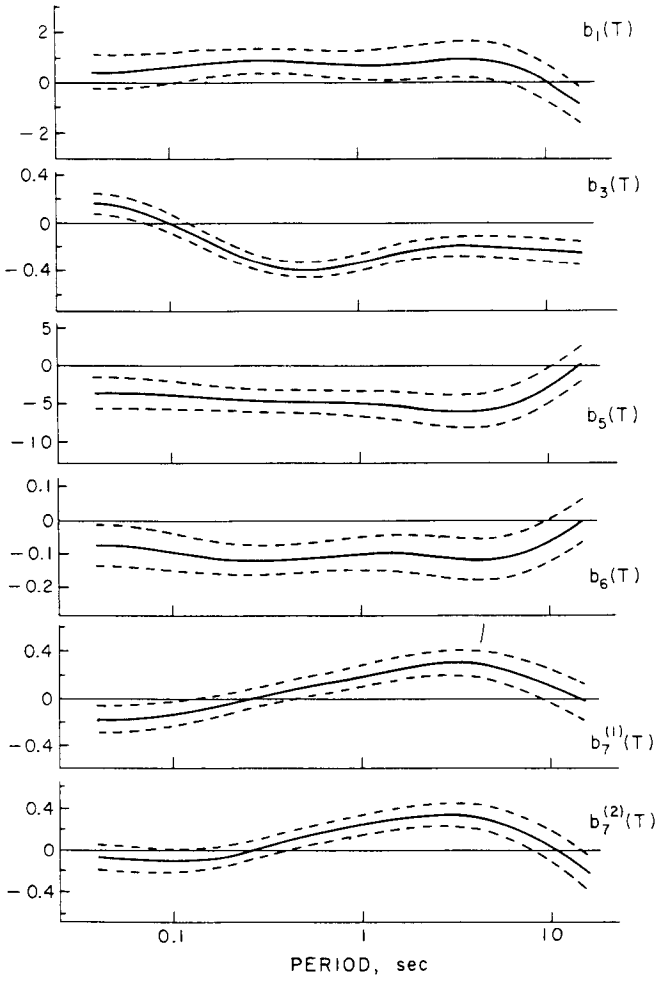

Figure 9. Functions $\hat{b}_1(T)$ (full lines) in equation (19) and the estimates of their 90 per cent confidence intervals (dashed lines)

The residues $\varepsilon(T)=\log_{10} \mathrm{FS}(T)-\log_{10} \widehat{\mathrm{FS}}(T)$ describing the distribution of the recorded $\mathrm{FS}(T)$ about the estimated $\widehat{\mathrm{FS}}(T)$ are next calculated. Figure 10 shows the plot of the residue levels corresponding to $p^*(\varepsilon, T) = 0{\cdot}1$ to $0{\cdot}9$ for $\log_{10} \mathrm{FS}(T)$. Refer to the corresponding Figure 2 for a complete description of each of nine sets off curves. As before, $\varepsilon(T)$ can be described by a normal distribution function with mean $\mu(T)$ and standard deviation $\sigma(T)$. Figure 11 shows the plot of the statistical parameters in the description of the residues, namely, $\hat{\mu}(T)$, $\hat{\sigma}(T)$, $\hat{\chi}^2(T)$ and $\mathrm{KS}(T)$. The trends shown in both figures are very similar to those (Figures 2 and 3) in the first part of the work.

DISCUSSION AND CONCLUSIONS

The aim of this paper has been to extend and to improve the previous scaling equations in the parametric representation of the Fourier spectral amplitudes of the observed strong earthquake ground motions. The functional forms of the empirical equations we used are not new, but have evolved, with minor refinements, from our previous work.[11, 12, 14, 15] The idea, which has been introduced here for the first time was to use the local soil and the local geologic characteristics of the site simultaneously in the development of the regression models. Also, the term hv, reflecting the directional dependence of the amplification, has not been employed in

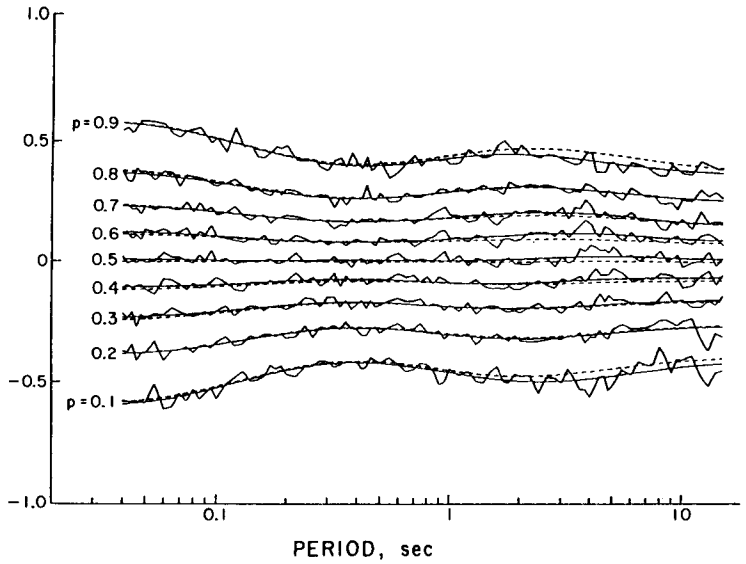

Figure 10. Distribution of residuals (irregular and smooth full lines) relative to the scaling model equation (19). Smooth dashed lines represent $p(\varepsilon, T)$ computed for equation (11) and are an approximation to $p^*(\varepsilon, T)$ (full lines)

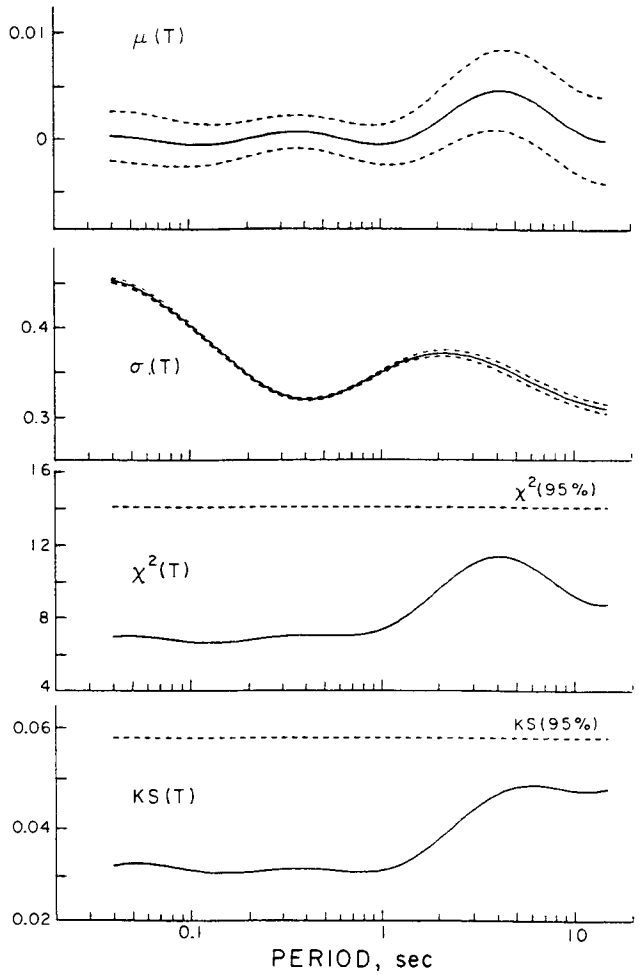

Figure 11. $\hat{\mu}(T)$ and $\hat{\sigma}(T)$ in equation (11) (full lines) and their 95 per cent confidence intervals (top two diagrams). Actual (full lines) and permissible (dashed lines), with 95 per cent confidence, amplitudes of $\chi^2(T)$ and Kolmogorov–Smirnov, KS(T) tests are shown in bottom two diagrams

our previous analyses. We found that the proposed model fits the data quite well and that there is consistency among different regression models.[23] No significant differences in the overall residual amplitudes have been observed between '1-step' and '2-step' regression models. Relative to our previous studies, the amplitudes of the residuals we found in this investigation are smaller.

To enable qualitative comparison of our results with some earlier investigations, which employed the local site characterization in terms of the local soil classification only, we carried out such analyses as well, by ignoring the local geologic features of the sites. Since the functional form of the dependence of the spectral amplitudes on the depth of sediments is similar to its dependence on the local soil conditions, we found that ignoring the local geologic conditions may lead to exaggerated amplitude factors 'representing' the local soil conditions. We conclude that both the local soil and the local geologic site conditions must be used together in the selection of the site spectific Fourier amplitude spectra.

One of the principal uses of the above new regression models is expected to be in the computation of uniform risk Fourier amplitude spectra for estimation of synthetic accelerograms[25, 26] and for various studies related to seismic microzonation.[27] For such applications the databases on earthquake occurrence in terms of the available catalogues are essential and must be used for as long time windows as the completeness and uniformity of the catalogues would allow. Therefore, as in our previous studies of spectral amplitudes,[13-15] and for practical reasons, constrained by the availability of data, we have used the published magnitudes, M, rather than some specific instrumentally or physically defined scale. For example, for most earthquakes in our data base with $M < 6{\cdot}5$ to 7, the published M is essentially same as the local magnitude[17] scale M_L, and thus the variations in the use of such scaling parameters are expected to result in only minor changes of the resulting spectral amplitudes.

ACKNOWLEDGEMENTS

This work was initiated at the Department of Civil Engineering of University of Southern California. It was completed at the School of Civil Engineering, Kyoto University with generous support of the Japan Society for Promotion of Science. This support is gratefully acknowledged.

REFERENCES

1. N. Haskell, 'Crustal reflection of plane SH waves, *J. geophys. res.* **65**, 4147–4150 (1960).
2. N. C. Tsai, 'Influence of local geology on earthquake ground motion', Earthquake Engineering Research Laboratory, California Institute of Technology, Pasadena, CA, 1969.
3. M. D. Trifunac, 'Surface motion of semi-cylindrical alluvial valley for incident plane SH waves, *Bull. seism. soc. Am.* **61**, 1755–1170 (1971).
4. K. Kanai, 'Relation between the earthquake damage of non-wooden buildings and the nature of the ground', *Bull. earthquake res. inst.* Tokyo University **27**, 97 (1949).
5. K. Kanai, 'Relation between the earthquake damage of non-wooden buildings and the nature of the ground', *Bull. earthquake res. inst.* Tokyo University **29**, 209 (1951).
6. B. Gutenberg, 'Effects of ground on earthquake motion', *Bull. seism. soc. Am.* **47**, 221–520 (1957).
7. C. M. Duke, 'Effects of ground on destructiveness of large earthquakes', *J. soil mech. found. div. ASCE* **84**, No. SM3, 1730 (1–23) (1958).
8. S. V. Medvedev, 'Ocenka seizmicheskoi balnosti u zavisimosti ot gruntovih uslovi', *Tr. geofiz. inst. AN SSSR* No. 4 (141) (1955).
9. Xi-Yuan Zhou, 'Effect of soil classification on structural damage during strong-motion earthquakes', Earthquake Engineering Research Report, Vol. II, Institute of Engineering Mechanics, Academia Sinica, Harbin, China, 1965, pp. 97–43.
10. H. B. Seed, C. Ugas and J. Lysmer, 'Site dependent spectra for earthquake resistant design', *Report No. EERC 74–12*, Earthquake Engineering Research Center, University of California, Berkeley, CA, 1974.
11. M. D. Trifunac, 'Preliminary empirical model for scaling Fourier amplitude spectra of strong ground acceleration in terms of earthquake magnitude, source of station distance and recording state conditions', *Bull. seism. soc. Am.* **66**, 1343–1373 (1976).
12. M. D. Trifunac, 'Preliminary empirical model for scaling Fourier amplitude spectra of strong motion acceleration in terms of Modified Mercalli Intensity and geologic site conditions', *Earthquake eng. struct. dyn.* **7**, 63–74 (1979).
13. M. D. Trifunac and V. W. Lee, 'Frequency dependent attenuation of strong earthquake ground motion', *Int. j. soil dyn. earthquake eng.* (in press).
14. M. D. Trifunac and V. W. Lee. 'Empirical models for scaling Fourier amplitude spectra of strong ground acceleration in terms of earthquake magnitude source of station distance, site intensity and recording site conditions', *Int. j. soil dyn. earthquake eng.* (in press).
15. M. D. Trifunac and V. W. Lee, 'Empirical models for scaling pseudo relative velocity spectra of strong earthquake accelerations in terms of magnitude, distance, site intensity and recording site conditions', *Int. j. soil dyn. earthquake eng.* (in press).
16. A. A. Gusev, 'Descriptive statistical model of earthquake source radiation and its application to an estimation of short period strong motion, *Geophys. j. roy. astr. soc.* **74**, 787–808 (1983).
17. C. F. Richter, *Elementary Seismology*, Freeman., San Francisco, 1958.

18. V. W. Lee and M. D. Trifunac, 'Attenuation of Modified Mercalli Intensity for small epicentral distance in California', *Report No. CE 85–01*, Department of Civil Engineering, University of Southern California, Los Angeles, CA, 1985.
19. H. B. Seed, C. Ugas and J. Lysmer, 'Site dependent spectra for earthquake resistant design', *Bull. seism. soc. Am.* **66**, 221–243 (1976).
20. D. C. Montgomery and E. A. Peck (Editors), *Introduction to Linear Regression Analysis*, Wiley, New York, 1982.
21. M. D. Trifunac and V. W. Lee, 'Preliminary empirical model for scaling Fourier amplitude spectra of strong ground acceleration in terms of earthquake magnitude, source to station distance, site intensity and recording site conditions', *Report No. CE 85–03*, Department of Civil Engineering, University of Southern California, Los Angeles, CA, 1985.
22. M. D. Trifunac and V. W. Lee, 'Preliminary empirical model for scaling pseudo relative velocity spectra of strong earthquake accelerations in terms of magnitude distance, site intensity and recording site conditions', *Report No. CE 85–04*, Department of Civil Engineering, University of Southern California, Los Angeles, CA, 1985.
23. M. D. Trifunac, 'Inference of local soil and geologic site conditions on Fourier spectrum amplitudes of recorded strong motion accelerations', *Report No. CE 87–04*, Department of Civil Engineering, University of Southern California, Los Angeles, CA, 1987.
24. V. W. Lee and M. D. Trifunac, 'Strong earthquake ground motion data in EQUINFOS: Part 1', *Report No CE 82–01*, Department of Civil Engineering, University of Southern California, Los Angeles, CA, 1982.
25. V. W. Lee and M. D. Trifunac 'Torsional accelerograms, *Int. j. soil dyn. earthquake eng.* **4**, 132–139 (1985).
26. V. W. Lee and M. D. Trifunac 'Rocking strong earthquake accelerations', *Int. j soil dyn. earthquake eng.* **6**, 75–89 (1987).
27. V. W. Lee and M. D. Trifunac, 'Microzonation of a metropolitan area', *Report No. 87–02*, Department of Civil Engineering, University of Southern California, Los Angeles, CA, 1987.
28. M. D. Trifunac, 'Analysis of strong earthquake ground motion for prediction of response spectra', *Earthquake eng. struct. dyn.* **2**, 59–69 (1973).